Dalton Transactions

PAPER

View Article Online
View Journal

Check for updates

Cite this: DOI: 10.1039/d1dt00845e

Third time's the charm: intricate non-centrosymmetric polymorphism in *Ln*SiP_3 (*Ln* = La and Ce) induced by distortions of phosphorus square layers†

Georgiy Akopov, ‡[a,b] Justin Mark, ‡[a,b] Gayatri Viswanathan, ‡[a,b] Shannon J. Lee, [a,b] Brennan C. McBride, [b] Juyeon Won,[a,b] Frédéric A. Perras, [a] Alexander L. Paterson, [a] Bing Yuan,[c] Sabyasachi Sen, [c] Adedoyin N. Adeyemi,[b] Feng Zhang,[a,d] Cai-Zhuang Wang, [a,d] Kai-Ming Ho,[d] Gordon J. Miller[b] and Kirill Kovnir *[a,b]

Complex polymorphic relationships in the *Ln*SiP_3 (*Ln* = La and Ce) family of compounds are reported. An innovative synthetic method was developed to overcome differences in the reactivities of the rare-earth metal and refractory silicon with phosphorus. Reactions of atomically mixed *Ln* + Si with P allowed for selective control over the reaction outcomes resulting in targeted isolation of three new polymorphs of $LaSiP_3$ and two polymorphs of $CeSiP_3$. *In situ* X-ray diffraction studies revealed that the developed method bypasses formation of the thermodynamic dead-end, the binary SiP. Careful re-determination of the crystal structure ruled out the previously reported ordered centrosymmetric structure of $CeSiP_3$ and showed that the main *Ln*SiP_3 polymorphs crystallize in the non-centrosymmetric $Pna2_1$ and $Aea2$ space groups featuring distinct distortions of the regular P square net to yield either *cis*–*trans* 1D phosphorus chains ($Pna2_1$) or disordered-2D phosphorus layers ($Aea2$). The disordered 2D nature of the P layers in the $Aea2$ $LaSiP_3$ polymorph was confirmed by Raman spectroscopy. A unique centrosymmetric $P2_1/c$ polymorph was observed for $LaSiP_3$ and has a completely different crystal structure lacking P layers. Consecutive polymorphic transformations at increasing temperatures for $LaSiP_3$($Pna2_1 \rightarrow P2_1/c \rightarrow Aea2$) were derived from optimized synthetic profiles and confirmed by a combination of phonon computations and experimental *in situ* and *ex situ* annealings. Crystal structures of the $LaSiP_3$ polymorphs were verified *via* advanced solid state NMR analysis using ^{31}P MAS and $^{31}P\{^{139}La\}$ double resonance techniques. A combination of phonon and electronic structure calculations, NMR T_1 relaxation times, UV/Vis/NIR spectroscopy, and resistivity measurements revealed that all the reported polymorphs are semiconductors with resistivities and thermal conductivities strongly dependent on the degree of distortion of P square layers in the crystal structure. Reported here, non-centrosymmetric *Ln*SiP_3 polymorphs with tunable resistivity and thermal conductivity provide a platform for the development of novel functional materials with a wide range of applications.

Received 14th March 2021,
Accepted 30th March 2021

DOI: 10.1039/d1dt00845e

rsc.li/dalton

---

[a] *Ames Laboratory, U.S. Department of Energy, Ames, IA 50011, USA. E-mail: kovnir@iastate.edu*
[b] *Department of Chemistry, Iowa State University, Ames, IA 50011, USA*
[c] *Department of Materials Science and Engineering, University of California, Davis, Davis, CA 95616, USA*
[d] *Department of Physics and Astronomy, Iowa State University, Ames, IA 50011, USA*

† Electronic supplementary information (ESI) available: Experimental details including synthesis descriptions as well as methods, figures, and tables pertinent to characterization techniques used: powder and single crystal X-ray diffraction, 11-BM synchrotron powder XRD, 17-BM *in situ* powder XRD, scanning electron microscopy, energy dispersive X-ray spectroscopy, Raman spectroscopy, differential scanning calorimetry, DFT calculations, solid-state diffuse reflectance spectroscopy, transport property measurements. CCDC 2051281 ($LaSiP_3$-*Aea*2), 2051282 ($LaSiP_3$-$P2_1/c$), 2051283 ($LaSiP_3$-$Pna2_1$), 2051284 ($CeSiP_3$-*Aea*2) and 2051285 ($CeSiP_3$-$Pna2_1$). For ESI and crystallographic data in CIF or other electronic format see DOI: 10.1039/d1dt00845e

‡ These authors contributed equally.

Introduction

Various materials, including many main group elements, exhibit polymorphism: the ability of a substance to crystallize in different structures while having the same chemical composition. The most famous example of elemental polymorphism is that of carbon. Graphite, a relatively soft allotrope of carbon, crystallizes in a layered structure with good thermal and electrical conductivities while diamond, the hardest naturally occurring material, adopts a structure with a 3D tetrahedral net of carbon atoms and is a wide bandgap insulator. Besides carbon, examples of polymorphism are known for many elements such as phosphorus (white, red, violet and black forms) and boron (α-, β-, and high pressure γ- and δ-forms).

Selective control in the synthesis of specific polymorphs is extremely important in chemistry, materials science, mineralogy, and pharmaceutics as the underlying differences in the crystal structures of polymorphs result in vastly different physical and electronic properties. In addition to elements, polymorphism is observed in simple binary compounds like boron nitride (BN) which can exist in the cubic and hexagonal form.[1–3] Hexagonal BN, the more stable form, is an interesting 2D material with a structure similar to that of graphite. It can be used as a lubricant and is studied for its optical properties.[1,4] Cubic BN, the high-pressure and high-temperature form, however is second only to diamond in hardness with a Vickers Hardness of 60–75 GPa.[2,5,6] Another recently studied polymorphic binary is NiP_2, in which the metallic cubic form exhibits superior electrocatalytic properties for the water splitting reaction than its semiconducting monoclinic counterpart.[7]

Polymorphism is also present in ternary and multinary phases; however, properties characterization is scarce because the synthesis of single-phase samples becomes increasingly challenging.[8–12] One such example is a family of ternary metal-silicon-phosphides $CeSiP_3$. There are several reports regarding the crystal structures of these phases, but there are significant disagreements on the exact symmetry of the various polymorphs.[13–15] Employing an innovative synthetic technique, we have been able to overcome solid–solid diffusion barriers and achieve high selectivity in the bulk synthesis of desired polymorphs for $CeSiP_3$ and the growth of its single crystals for redetermination of crystal structures. Applying this technique to the less-studied La–Si–P phase space resulted in the discovery of three novel polymorphs. In the $LaSiP_3$ system, the high- and low-temperature polymorphs are non-centrosymmetric and structurally related while the intermediate-temperature polymorph has a completely different centrosymmetric crystal structure. The non-centrosymmetric polymorphs of $LaSiP_3$ and $CeSiP_3$ reported here crystallize in similar structures which differ in the degree of distortion of their planar square nets of P atoms. Structures containing such square nets are of significance due to their potential for topological properties. Unlike the title compounds, a vast majority of materials containing topological square nets are centrosymmetric.[16,17] Breaking of the inversion symmetry results in spin–orbit coupling which splits the Fermi surface by removing the spin degeneracy of electrons and potentially changes the band structure topology.

In this work, we report an innovative synthetic method, followed by detailed *in situ* X-ray diffraction studies of the synthetic mechanism of $Ln\mathrm{SiP}_3$ which culminated in a high degree of selective control in polymorphic transformations. The structures of the P fragments were confirmed by advanced ^{31}P/^{139}La solid state NMR spectroscopy. Detailed electronic and phonon computations, heat and charge transport measurements, and optical spectroscopy illuminated the semiconducting nature of the five new $Ln\mathrm{SiP}_3$ (Ln = La, Ce) compounds which exhibit ultra-low thermal conductivities which depend on the degree of the distortion of their P square nets.

Experimental methods

A detailed description of synthetic, characterization, and analysis methods are provided in ESI.† Bulk powders of the different polymorphs of $Ln\mathrm{SiP}_3$ (Ln = La and Ce) were prepared using pre-arc-melted LaSi or CeSi precursors and phosphorus, while crystal growth was achieved using a Sn flux synthesis from either the elements or a pre-arc-melted precursor, as well as a flux-free synthesis from a pre-arc-melted precursor.

HAZARD: *The amount of P in any reaction container should be kept to a minimum because at relatively high temperatures during synthesis the resulting vapor pressure of P may be sufficient to cause the sealed ampoule to shatter or explode!*

Synthesized phases were analyzed by laboratory powder and single crystal X-ray diffraction (PXRD and SCXRD); synchrotron high-resolution and *in situ* PXRD at the 11-BM and 17-BM beamlines at the Advanced Photon Source at Argonne National Lab (APS ANL); ^{31}P and ^{139}La solid state nuclear magnetic resonance (NMR) spectroscopy; Raman spectroscopy; scanning electron microscopy/energy dispersive spectroscopy (SEM/EDS); and differential scanning calorimetry (DSC). Electronic structure calculations using density functional theory (DFT) were employed to examine the electronic properties and dynamic stability of the synthesized phases. Transport properties were measured using a physical property measurement system (PPMS) on high density pellets that were pressed using spark plasma sintering (SPS). Optical bandgaps were measured using a UV/Vis/NIR spectrophotometer.

Results and discussion

Crystal structure

$CeSiP_3$ was first reported in 1975 to crystallize in the $Cm2a$ or $Cmma$ space groups.[14] In 1976, it was reported to have $Pn2_1a$ (a nonstandard setting of $Pna2_1$) or $Pnma$ space group symmetry, and then redetermined several years later to crystallize in the $Pn2_1a$ space group.[13,15] No crystal structures were reported for the La and Pr analogues, but formation of phases similar to $CeSiP_3$ was identified by powder XRD.[13] The crystal structure of a single ternary phase was already reported in the La–Si–P phase space, $LaSi_2P_6$.[18] Here we report three new polymorphs in this system. Two of the $LaSiP_3$ polymorphs exhibit related non-centrosymmetric structures and crystallize in the primitive and base-centered orthorhombic space groups $Pna2_1$ (No. 33) and $Aea2$ (No. 41), respectively, while the third polymorph of $LaSiP_3$ crystallizes in the distinctly different centrosymmetric primitive monoclinic space group $P2_1/c$ (No. 14) (Fig. 1 and 2).

The non-centrosymmetric $Pna2_1$ and $Aea2$ polymorphs have related structures with the primary difference being in their planar phosphorus layers as well as the significant degree of disorder in the $Aea2$ structure. Both crystal structures are composed of the following layers stacked along the [010] direction: La, double-tetrahedral [SiP_2], La, and flat P layers. The double-tetrahedral layers are composed of corner-sharing SiP_4 tetrahedra and are surrounded above and below by nearly planar square nets of La atoms. Within the La layers, the La–La distances exceed 4.00 Å. Adjacent lanthanum layers are separated by planar P nets, which can be considered distortions from an ideal square net of P atoms.

In the $Pna2_1$ polymorph, the planar P layers contain 1D *cis–trans* chains of P atoms along the [001] direction. P–P distances

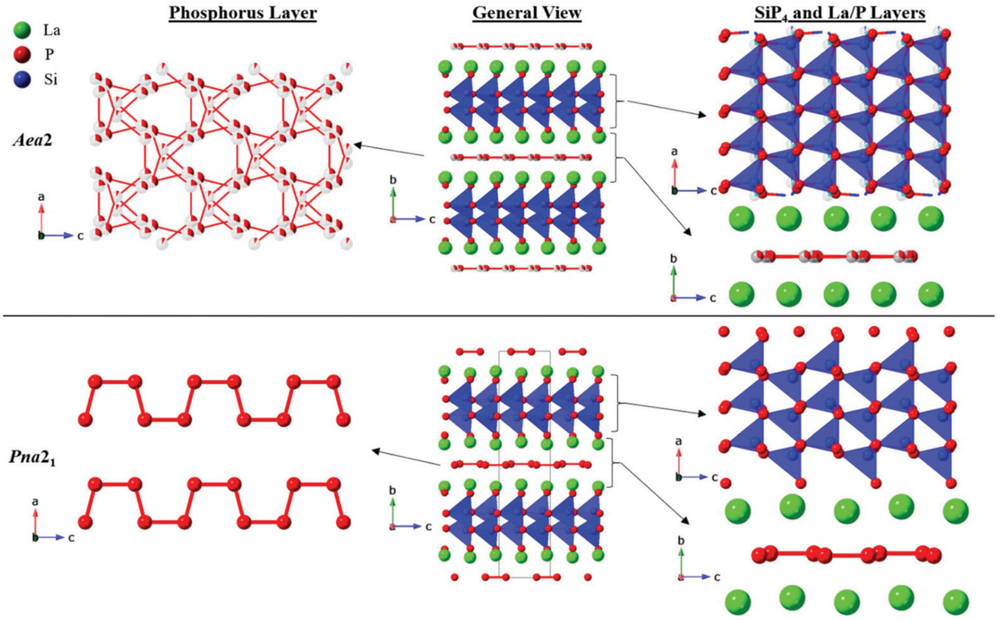

Fig. 1 Crystal structures of the two non-centrosymmetric polymorphs of $LaSiP_3$: (top) high-temperature $Aea2$ and (bottom) low-temperature $Pna2_1$. For the P layers, P–P bonds (lines connecting P atoms) are shown for distances in the range of 2.1–2.5 Å. Element legend: La – green; Si (atoms and tetrahedra) – blue; P – red (with partial occupancy).

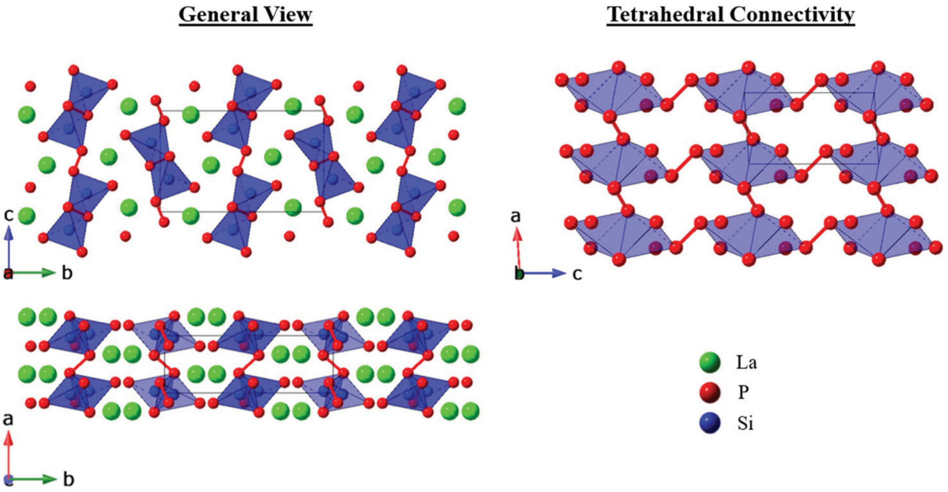

Fig. 2 Crystal structure of the intermediate-temperature polymorph $LaSiP_3$ ($P2_1/c$) showing a general view as well as SiP_4 tetrahedral connectivity. Element legend: La – green; Si (atoms and tetrahedra) – blue; P – red.

within the chains are 2.26–2.30 Å which are comparable to the single covalent inter-phosphorus bonds found in many phosphides, while inter-phosphorus distances between neighboring chains in the structure exceed 3.7 Å, indicating no covalent interactions.[8,9,19–22] Similar distortions of square nets with hypervalent pnictides and chalcogenides into *cis–trans* 1D chains have been predicted and experimentally observed, primarily for heavier main group elements such as Sb and Te.[16,23–26]

The *Aea*2 structure of $LaSiP_3$ differs from the *Pna*2_1 version in the apparent distortion of the P layer. Instead of ordered *cis–trans* chains, the P layers in the *Aea*2 polymorph form disordered square nets which can be considered as superposition of several possible distortions from the ideal square net (Fig. 1). An ideal square net of P atoms would result in unreasonably long P–P distances of approximately 3 Å, while the longest reported P–P distances in regular, undistorted P square nets are 2.7 Å.[27,28] The P sites within this layer are split into four different crystallographic positions with occupancies ranging from 8% to 38%. The observed P layer site splitting in the *Aea*2 structure results in a wide distribution of shorter interatomic P–P distances ranging 2.0–2.9 Å. While a single covalent P–P bond is close to 2.2 Å, significantly longer P–P distances have been reported in metal phosphides.[21,27,28] The P net shown in Fig. 1 was plotted with reasonable P–P covalent distances of 2.1–2.5 Å. The view of this net may be altered if longer P–P separation (2.5 Å and 2.7 Å) are included (Fig. S19†). This disordered P layer may seem like a superposition of several *cis–trans* P chain running in different directions, but spectroscopic Raman and NMR studies do not support such a simplified description. The *Aea*2 phase also displays disorder in the $[SiP_2]$ double-tetrahedral layer in which, in addition to the sites found in *Pna*2_1, the layer contains additional split Si and P positions that account for approximately 5% of the atoms in the double-tetrahedral layer.

Layers of La atoms in these two non-centrosymmetric polymorphs are staggered along the [010] direction of the unit cell in an …*ABBA*… arrangement and are 'held-in-place' by the rigid $[SiP_2]$ double-tetrahedral layers. The La layers in the two polymorphs distinctly differ when looking along the [100] direction: La atoms are flat in the *Aea*2 structure, but there is mild corrugation in the *Pna*2_1 structure (Fig. S11a and b†). In the *Pna*2_1 polymorph, the corner-connected tetrahedra of the $[SiP_2]$ double-tetrahedral layers allow for little flexibility within the La layers. To compensate for this rigidity and the ordered P layer, the La atoms displace slightly above or below the plane. However, in the *Aea*2 polymorph, the disordered P layers and mildly disordered double-tetrahedral layers provide enough degrees of freedom for the La atoms to sit completely within the plane.

In both of these structures La is surrounded by 9 P atoms (assuming the idealized P sites are used for the disordered planar P nets in the *Aea*2 polymorph), but the local environments of La atoms differ slightly due to small displacements of the La atoms in the *Pna*2_1 polymorph. The subscripts *dtet* and *plane* are used to distinguish P atoms of the double tetrahedral layer and planar phosphorus layer, respectively. La–P_{plane} distances range from 2.983(3)–3.299(3) Å in the *Pna*2_1 structure and 2.87(1)–3.50(1) Å in the *Aea*2 phase. The somewhat wider range of distances observed in the *Aea*2 polymorph can be attributed to the disorder within the P layers. However, when La–P_{dtet} distances from the $[SiP_2]$ double-tetrahedral layer are considered, the distribution of interatomic distances is inversed: La–P_{dtet} distances are 3.004(4)–3.120(1) Å in the *Aea*2 polymorph, but range from 2.955(4)–3.148(1) Å in *Pna*2_1 structure.

The structure of the P layer in the *Aea*2 case could be assumed to be an averaged superposition of several P-layers, composed of P chains going in two orthogonal directions instead of the disordered square net layer. If this assumption is correct, the spectroscopic signatures of P–P layers are expected to be similar for *Pna*2_1 and *Aea*2 polymorphs. However, the Raman spectra of these two polymorphs of $LaSiP_3$ show a significant difference in the P–P stretching band (Fig. S18†). For the *Pna*2_1 $LaSiP_3$ polymorph, the band at ~320 cm^{-1} corresponding to the P–P stretching in the 1D P chains is broader than the bands below 200 cm^{-1} corresponding to vibrational modes associated with Si–P and La–P bonds. The corresponding P–P stretching band for the *Aea*2 polymorph centered at ~323 cm^{-1} is three times wider (full-width-at-half-maximum FWHM ~50 cm^{-1}) than that in the spectrum of the *Pna*2_1 polymorph (FWHM ~17 cm^{-1}). Such substantial broadening of this band for the *Aea*2 polymorph rules out a simple picture of the P layer as a superposition of locally ordered 1D P chains running in two orthogonal directions. The ^{31}P solid state NMR spectra discussed below also indicate significant differences between the structures of the *Pna*2_1 and the *Aea*2 polymorphs.

The *Pna*2_1 structure of $LaSiP_3$ can be derived from the *Aea*2 structure by a *klassengleiche* transformation of index 2 that splits the 8*b* Wyckoff positions in *Aea*2 into two distinct sets of 4*a* sites. In *Ln*SiP_3 (*Ln* = La, Ce), this results in twice as many sites for *Ln*, Si, and P in the lower symmetry *Pna*2_1 structure as the *Aea*2 polymorph (Fig. S12†).

Single crystals acquired from the initial synthesis of the $CeSiP_3$ sample confirmed the previously reported structural model with space group *Pna*2_1,[15] but the powder diffraction pattern of this phase contained several unassigned peaks. This result, in combination with the discovery of the three new $LaSiP_3$ polymorphs, led to a more detailed synthetic investigation resulting in the discovery of a new polymorph of $CeSiP_3$ crystallizing in the *Aea*2 space group. The crystal structures of the $CeSiP_3$ polymorphs are analogous to $LaSiP_3$ apart from the $P2_1/c$ polymorph, which exists for $LaSiP_3$ only. The *Pna*2_1 phase of $CeSiP_3$ is completely ordered while the *Aea*2 phase exhibits a higher degree of disorder in SiP_2 double tetrahedral layer then the La analogue due to overall contraction of the unit cell arising from the smaller size of the Ce cation, although the P layer in *Aea*2 $CeSiP_3$ polymorph can be described with only three split P sites.

The $P2_1/c$ polymorph was only observed for $LaSiP_3$ and all attempts to synthesize this polymorph for Ce resulted in formation of either the *Pna*2_1 or *Aea*2 phases. The crystal structure of $P2_1/c$ $LaSiP_3$ is composed of only two types of layers –

alternating La and [Si_2P_6] double tetrahedral layers (with differing inter-connectivity from the other polymorphs) in which the shortest La–P distances are 2.9892(8) Å. SiP_4 tetrahedra share edges to form Si_2P_6 units with Si–P distances of 2.186(1)–2.321(1) Å. These units are interconnected *via* P–P bonds of 2.197(2) Å and 2.217(2) Å propagating along the [100] and [001] directions, respectively, to form the [Si_2P_6] layers. Inter-phosphorus bonds that connect neighboring tetrahedra have also been observed in the polymorphs of Ba_2SiP_4 and La_2SiP_4.[8,9,20,29] In particular, tetragonal AE_2SiP_4 (*AE* = Sr, Eu, Ba) involves single tetrahedra bonded by P–P bonds to form a 3D framework,[8,9,20] while orthorhombic Ba_2SiP_4 and La_2SiP_4 contain chains of single SiP_4 tetrahedra bonded through P–P bonds to neighboring tetrahedra.[9,29] With the compounds reported here, as well as $LaSi_2P_6$ and La_2SiP_4,[29] 3 out of 5 compounds in the La–Si–P phase space are non-centrosymmetric (NCS). This high abundance of NCS structures in a single system is not observed in binary metal pnictides or silicides, where the amount of NCS compounds is less than 10%. However, silicide-pnictides of alkaline-earth metals exhibit similar high abundance of NCS structures such as Mg–Si–As (2 out of 3 are NCS)[22,30] and Ba–Si–P (3 out of 5 are NCS).[8,9,19,20,31,32] We hypothesize that the ability of Si–P and Si–As substructures to provide flexible coordination environments to electropositive metals, due to multiple binding modes and localized electron lone-pairs on pnictogen atoms, is crucial for generation of such NCS structures in metal–tetrel–pnictide systems.

Synthesis

Bulk powder samples of $LnSiP_3$ were prepared using precursor metal silicides (Fig. S1†) and stoichiometric molar quantities of phosphorus, *Ln*Si:3P, with no flux and with the dwell times and temperature profiles summarized in Table 1. The main synthetic challenge comes from the high difference in reactivities between *Ln*, Si, and P due to high melting point of silicon (1410 °C) compared to the melting point of the lanthanides (La: 920 °C; Ce: 800 °C) and phosphorus sublimation temperature (400–600 °C). Traditional solid-state reactions of the elements, *Ln* + Si + 3P, at elevated temperatures did not yield ternary phases but, instead, resulted in preferential formation of *Ln*P and SiP binaries, which do not react with one another due to slow solid–solid diffusion.

To make silicon more reactive, it was first arc melted with *Ln* to form the binary compound *Ln*Si. Arc-melted precursors chosen in this study, have higher temperature stability than Si with melting points of 1620–1630 °C. Nevertheless, such precursors react with P at temperatures as low as 650 °C (Fig. 3). We hypothesize that the main advantage of the *Ln*Si precursors is the spatial proximity of *Ln* and Si atoms which may facilitate formation of ternary phase rather than a mixture of two separate binaries due to minimized diffusion limitations. As shown below by *in situ* studies a reaction of *Ln*Si with phosphorus vapor directly forms a ternary phase and bypass formation of SiP.

Table 1 Optimized synthetic conditions (maximum temperature/dwell time) for the different polymorphs of $LnSiP_3$ (*Ln* = La and Ce) resulting in highest yield of targeted products. All reactions were conducted with a 12 h heating to maximum temperature and a 10 h cooling to room temperature

Polymorph	$LaSiP_3$	$CeSiP_3$
*Aea*2	1050 °C/0 h	1050 °C/0 h
$P2_1/c$	900 °C/240 h	N/A
$Pna2_1$	750 °C/240 h	900 °C/240 h

In situ synchrotron PXRD experiments shed light on the formation mechanism of $LnSiP_3$. Fig. 3 shows the results of an *in situ* study of $LaSiP_3$ formation from the LaSi precursor and phosphorus in a 1 : 3 molar ratio. The LaSi precursor (Fig. S1†) was prepared by arc-melting La and Si in a 1 : 1.05 molar ratio, and the excess of Si accounts for the minor presence of La_2Si_3 in the starting materials. The low temperature polymorph ($Pna2_1$) together with LaP forms above 650 °C *via* direct conversion of lanthanum silicide into a lanthanum silicon phosphide, no intermediate silicon-containing phases were detected with temperature resolution of ~1 °C. This is contrast with reaction of elements (La + Si + 3P) where SiP binary is observed in reaction products of all reactions carried at different temperatures, 750–1100 °C.

As the temperature increases further, a transformation to the high temperature polymorph (*Aea*2) can be observed above 760 °C. No further transformations upon cooling were observed and, as a result, the cooling rate for this non-flux reaction is not crucial for synthesis. The $P2_1/c$ $LaSiP_3$ polymorph is not observed during this short ~2 h synchrotron experiment, which is in line with *ex situ* experiments that suggest optimal synthesis of this phase requires long annealing times. The $CeSiP_3$ system behaves in a similar manner to $LaSiP_3$, as shown in Fig. S2,† whereby a CeSi precursor reacts with phosphorus to form the ternary polymorphs at temperatures above 730 °C. *In situ* experiments resulted in the formation of LaP and CeP in addition to the ternary phases due to the fast rate of these reactions compared to bulk synthesis and the possibility of being off-stoichiometry due to sample loading in a capillary. In the laboratory *ex situ* syntheses where proper mixing of correct ratio of LaSi precursor and P was achieved the LaP admixture was minimized (Fig. 4).

Selective *ex situ* synthesis of clean bulk powders requires that the appropriate temperature and dwell time profiles be followed (Fig. 4 and Table 1). The high-temperature *Aea*2 polymorph readily forms above 1000 °C and requires no dwell time. High resolution synchrotron powder data for $LaSiP_3$ clearly shows that despite similarities between the crystal structures of the *Aea*2 and $Pna2_1$ polymorphs, the phases possess clearly distinguishable powder patterns (Fig. S3A and B†). The low-temperature $Pna2_1$ polymorphs for both rare earth metals require significantly longer synthesis time due to a lower temperature of formation (Fig. 4). The third polymorph, monoclinic $P2_1/c$, can be prepared by annealing LaSi and phosphorus at 900 °C over 240 hours (Fig. S4†). Further annealing of $P2_1/c$ product at a higher temperature resulted in formation of mainly the *Aea*2 polymorph. Long time annealing

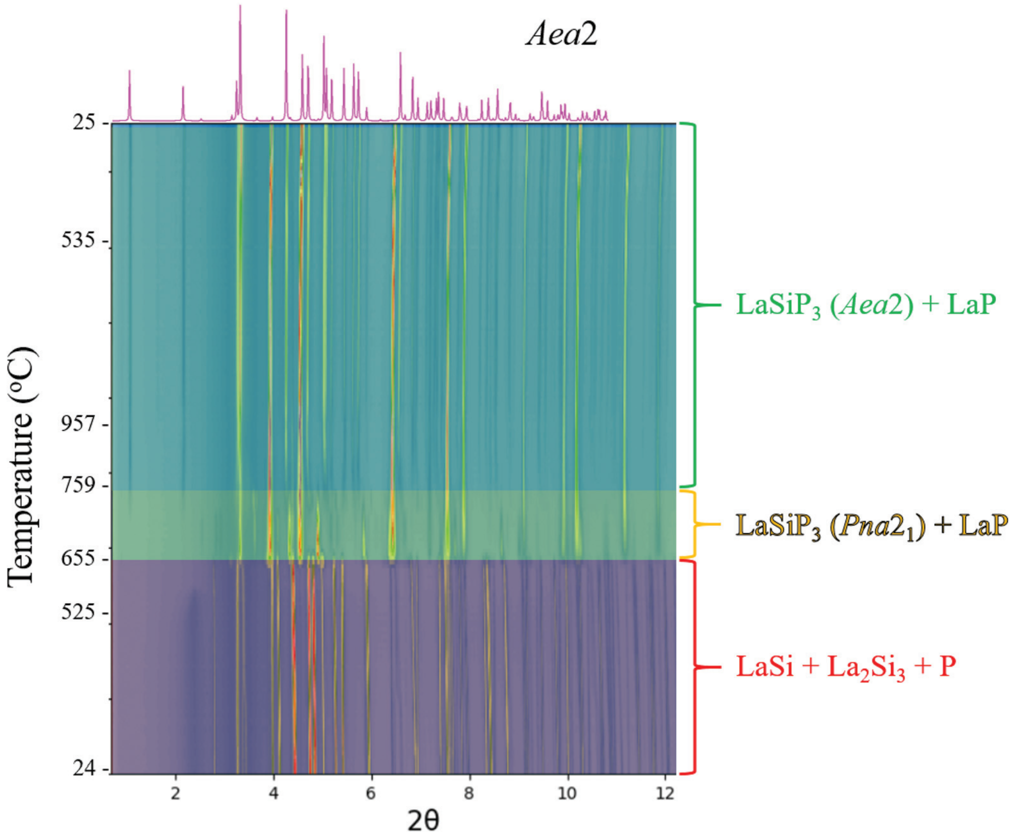

Fig. 3 *In situ* PXRD patterns showing phase formation in the $LaSiP_3$ system collected at the 17-BM beamline at Argonne National Lab. The pre-arc-melted LaSi and P reactants form $LaSiP_3$ (*Pna*2_1) at ~650 °C followed by a transformation to $LaSiP_3$ (*Aea*2) above 760 °C. Synchrotron X-ray wavelength $\lambda = 0.24158$ Å.

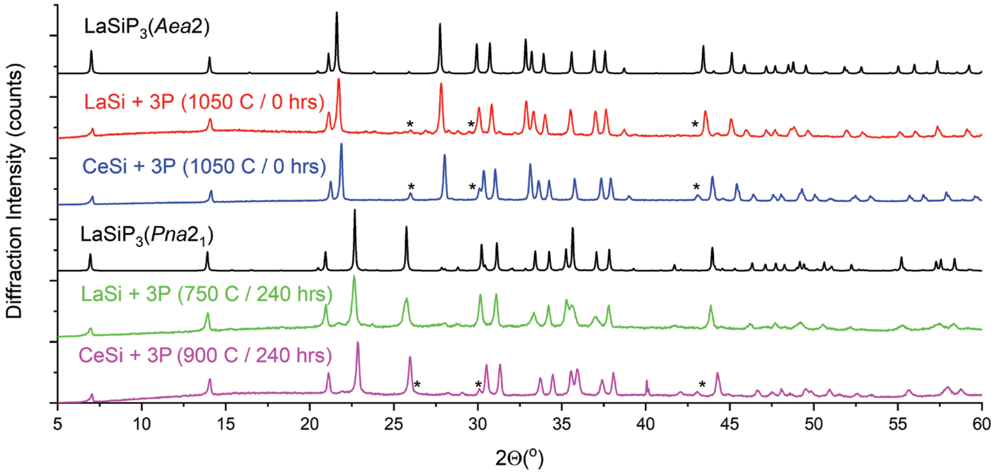

Fig. 4 PXRD patterns showing phase formation and polymorphism for *Ln*SiP_3 (*Ln* = La and Ce). *Aea*2 polymorphs for both lanthanides were synthesized at 1050 °C with no dwell time, while the *Pna*2_1 phases were synthesized at 750 and 900 °C for La and Ce, respectively, with a dwell time of 240 h. Patterns in black are calculated from the single crystal structural models; patterns in color are experimental. (*) denotes peaks corresponding to LaP and CeP phases.

of the *Aea*2 polymorph at temperatures above 1000 °C resulted in the decomposition of $LaSiP_3$ and formation of yet another ternary compound, La_2SiP_4.[29] This indicated metastable nature of the *Aea*2 $LaSiP_3$ polymorph.

$CeSiP_3$ polymorphs can be prepared in a similar manner starting from CeSi, although CeP becomes a prominent secondary phase (Fig. 4). Our screening of the other rare-earth elements shows that the *Ln*SiP_3 ternary phase forms for Pr and

Nd, although *Ln*P binary become major phase, while the formation of *Ln*SiP_3 was not observed for Sm and Gd with the synthesis resulting in a mixture of binary phosphides (Fig. S5†).

Both *in situ* and *ex situ* annealing experiments show that the low temperature polymorphs of *Ln*SiP_3 can be transformed into the high temperature ones by reannealing the samples at a higher temperature. Fig. 5 shows the 17-BM diffraction experiment for a transformation of $CeSiP_3$ from *Pna*2_1 to *Aea*2 at temperatures above 980 °C. Similar experiments can be conducted on a larger scale; for example, the *ex situ* reannealing of a *Pna*2_1 $LaSiP_3$ sample at 1000 °C transforms it to the high temperature *Aea*2 polymorph (Fig. S6†).

DSC

Differential scanning calorimetry experiments were hampered by the reaction of the $LaSiP_3$ melt with the silica DSC ampoule, resulting in the formation of $La_2Si_2O_7$ (Fig. S7†). An endothermic event, which may correspond to melting of $LaSiP_3$, was observed at 1035 °C. For the $CeSiP_3$ sample, which contained a mixture of the *Pna*2_1 and *Aea*2 polymorphs, events corresponding to typical congruently melting and crystallization were observed at 1033 °C and 1011 °C, correspondingly. PXRD confirms the presence of only the high-temperature *Aea*2 polymorph after the DSC experiment (Fig. S7† bottom). This agrees with synthetic results in which long time annealing at low temperatures were required to stabilize the *Pna*2_1 polymorph.

SEM/EDS

Backscattered electron images (Fig. S8†) for all three polymorphs of $LaSiP_3$ confirm the samples to be majority ternary metal silicon phosphide. Further EDS analysis gave average compositions (normalized to 1 La atom) of $La_{1.00}Si_{1.11(3)}P_{2.95(6)}$ (*Aea*2), $La_{1.00}Si_{1.02(2)}P_{2.87(9)}$ for (*Pna*2_1), and $La_{1.00}Si_{1.04(7)}P_{2.71(9)}$ ($P2_1/c$) which are in good agreement with the nominal composition, $LaSiP_3$.

Electronic structure calculations

Vienna *Ab initio* Simulation Package (VASP) was used to calculate energy-optimized structures of the various $LaSiP_3$ polymorphs. Complete relaxation of the unit cell and atomic positions of the $P2_1/c$ and *Pna*2_1 polymorphs did not result in any significant distortions or changes to the crystal structure. Both polymorphs are predicted to be semiconductors with band-

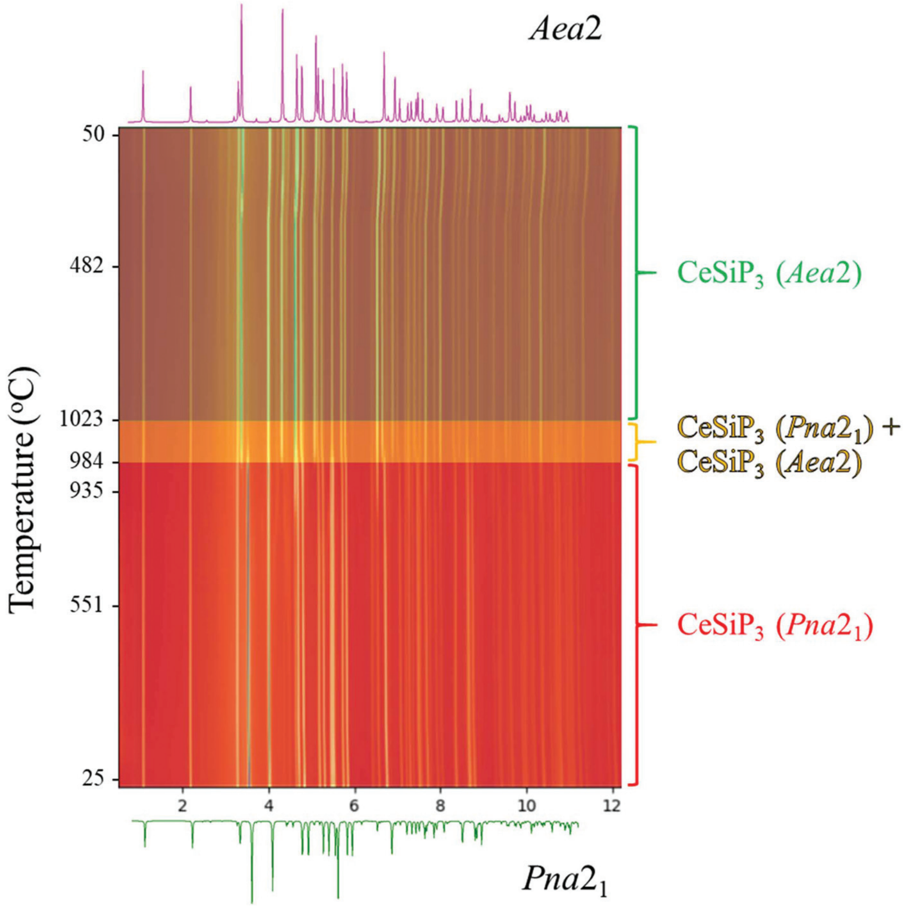

Fig. 5 *In situ* PXRD patterns showing phase transformation in the $CeSiP_3$ system collected at the 17-BM beamline at Argonne National Lab. $CeSiP_3$ (*Pna*2_1) transforms into $CeSiP_3$ (*Aea*2) above 980 °C. Synchrotron X-ray wavelength λ = 0.24153 Å.

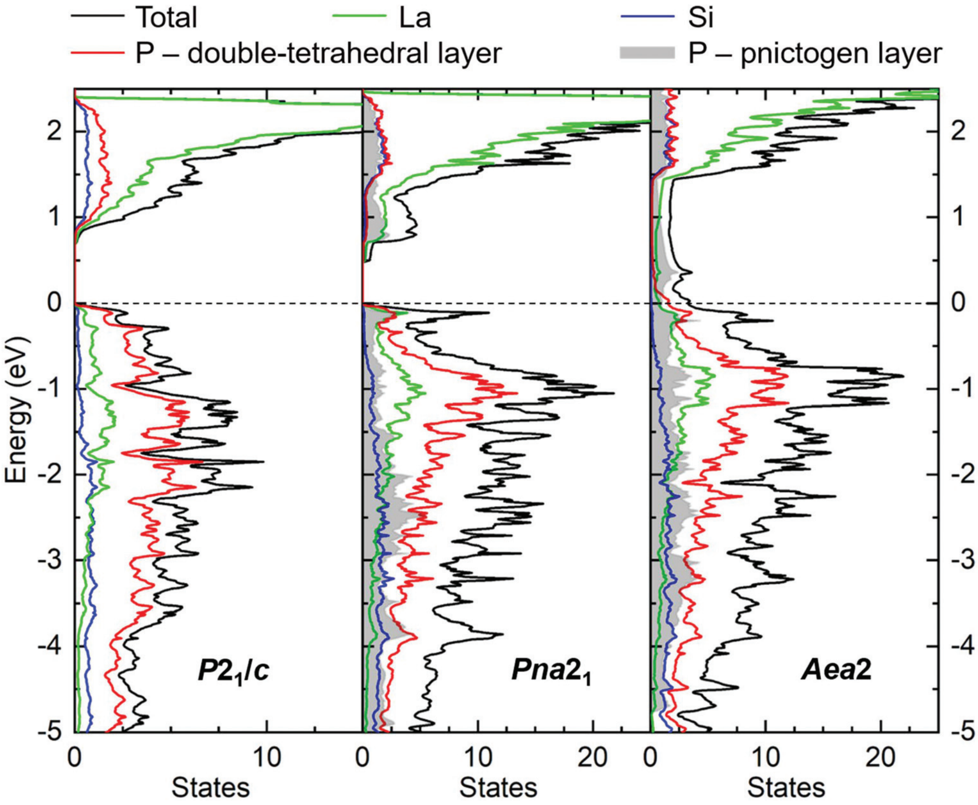

Fig. 6 Calculated DOS for three polymorphs of $LaSiP_3$ after complete structure relaxation using VASP: $P2_1/c$ (left), $Pna2_1$ (middle), $Aea2$ (right). For the latter polymorph, the fully relaxed P layer model shown in Fig. S13c† was used. The total DOS is shown by the black line and partial DOS curves are shown for La (green), Si (blue), and P (red and gray filled). The P states are divided into contributions from the $[SiP_2]$ double-tetrahedral layer (red) and the P layer (gray filled) for the $Pna2_1$ and $Aea2$ polymorphs. The Fermi level, indicated by the dashed black line, is the reference energy.

gaps of 0.7 eV ($P2_1/c$) and 0.5 eV ($Pna2_1$) (Fig. 6). Near the Fermi level, P states contribute most to the valence band with a visible contribution from La states. The contribution from Si states is similar to that of La states in the valence band at 2–3 eV below the Fermi level but tapers off when approaching the top of the valence band. La states dominate the lower regions of the conduction band with minor Si and P contributions.

The overall shape of the DOS for monoclinic $LaSiP_3$ resembles that of La_2SiP_4.[29] La–P orbital mixing in the upper region of the valence band is notable and is expected to strongly influence charge transport properties. For example, replacement of Ba with La in the clathrate $La_2Ba_6Cu_{16}P_{30}$ with similar La/P orbital mixing resulted in a an order of magnitude increase in hole mobility.[33] Unfortunately, attempts to study the transport properties of monoclinic $LaSiP_3$ were hampered by the inability to sinter a dense sample. Based on the computational results, a Zintl-type formulation can be proposed for this semiconducting phase. La adopts a formal charge of +3 and Si is assigned 0 because it is four-bonded to P atoms. The two types of P atoms are each assigned as −1 because they are two-bonded. One type of P bridges two Si atoms while the other type bonds to Si and another P atom. An alternative, completely ionic formulation $La^{3+}Si^{4+}(P^{2-})_2(P^{3-})$, differentiates these two P sites from those that form P–P bonds (2−) and those that bond only to Si (3−).

In the relaxed structure of $Pna2_1$ $LaSiP_3$ the *cis–trans* P chains are preserved with reasonable interatomic distances (blue and black lines in Fig. S13a†). However, unlike the $P2_1/c$ structure, $Pna2_1$ $LaSiP_3$ has P atoms in two distinct types of layers, *i.e.*, $[SiP_2]$ double-tetrahedral and planar pnictogen layers. The partial DOS curves reveal that P states in the double-tetrahedral layer primarily contribute to the valence band, especially intensifying at 0.5–3.0 eV below the Fermi level, while P states in the pnictogen layer contribute almost consistently throughout the valence and conduction bands. This broad dispersion of pnictogen states has been observed in the partial DOS for ZrSiS-type YbPS which also features a pnictogen layer of P atoms.[34] Again, Zintl-type and purely ionic formulations can be constructed for $Pna2_1$ $LaSiP_3$: $La^{3+}Si^{0}(P_{dtet}{}^{2-}P_{dtet}{}^{0})(P_{plane}{}^{1-})$ or $La^{3+}Si^{4+}(P_{dtet}{}^{3-})_2(P_{plane}{}^{1-})$. Here, the P atoms of the double tetrahedral layer (P_{dtet}) are bonded to either a single Si or used to corner-connect three SiP_4 tetrahedra. The semiconducting nature of this phase is supported by resistivity and diffuse reflectance measurements (*vide infra*).

Both the $P2_1/c$ and $Pna2_1$ polymorphs of $LaSiP_3$ show no computed imaginary phonon modes (Fig. S15†) indicating these two structures are dynamically stable. Fig. S16† gives the free energy difference between these two polymorphs as a function of the temperature. At T = 0, the free energy of the

$P2_1/c$ polymorph is only 2.5 meV per atom higher than that of the $Pna2_1$ polymorph, with the zero-point energy $\left(\frac{1}{2}\sum_{nk}\hbar\omega_{nk}\right)$ included. Calculations predict a phase transformation from the $Pna2_1$ to the $P2_1/c$ polymorph at $T = 374$ K. This transition temperature is lower than that observed experimentally suggesting a high kinetic barrier could exist between these two polymorphs.

The crystallographic disorder in the phosphorus layer of the $Aea2$ polymorph poses significant challenges from a computational perspective. Several ordered models constrained under the space group $Aea2$ were constructed to examine the possible electronic behavior of this phase as described in the ESI.† The fully relaxed model retains the $Aea2$ symmetry with reasonable unit cell lattice parameters (a = 5.9046 Å, b = 25.5768 Å, c = 5.7885 Å). However, a significant distortion of the flat pnictogen layer results in the formation of isolated P_2 dumbbells along the a-direction in a ladder-type substructure; this substructure is known to form as a result of a Peierls distortion in 2D square pnictogen sheets.[26] Phonon calculations show instability of this fully relaxed model of the $Aea2$ polymorph because of imaginary modes (Fig. S15†). The total energy at $T = 0$ for this model (−6.000 eV per atom) is significantly higher than that of the $P2_1/c$ (−6.042 eV per atom) and $Pna2_1$ (−6.045 eV per atom) polymorphs. These results demonstrate that $Aea2$ model with dumbbell-like P_2 dimers is an unrealistic oversimplification of the observed crystal structure, in agreement with the diffraction and spectroscopic experimental observations that P atoms form a more complex network in the *Aea2* polymorph. The DOS for the fully relaxed $Aea2$ model (Fig. 6) does not yield a bandgap which opposes the semiconducting behavior of this polymorph indicated by NMR T_1 relaxation times, as well as resistivity and diffuse reflectance measurements. All other considered $Aea2$ models also resulted in a metallic DOS (Fig. S14†). To fully explore the crystal structure of the $Aea2$ polymorph, further studies such as molecular dynamics simulations and high-resolution electron microscopy are required. The latter has been crucial in identifying the superstructure of complex polytellurides such as $K_{0.33}Ba_{0.67}AsTe_2$, $AMRETe_4$, ALn_3Te_8, and $RETe_3$ which were initially assumed to have much smaller unit cells.[35–38] These systems have been shown to undergo lattice distortions driven by electronic structure instead of maintaining a perfect square net of tellurium atoms; the result is the formation and unique sequencing of various oligomeric units that can be identified using electron microscopy techniques.[39]

Assuming the same ionic electron-counting scheme used for the other $LaSiP_3$ polymorphs, we can devise an electron-balanced Zintl formalism for the $Aea2$ polymorph of $LaSiP_3$. The assignments for La, Si, and P atoms of the double-tetrahedral layer are identical to the $Pna2_1$ polymorph. To maintain the electron-balanced composition, the disordered pnictogen layer must have an oxidation state of −1 yielding a Zintl composition of $La^{3+}Si^{4+}(P_{dtet}{}^{3-})_2P_{plane}{}^{1-}$ or $La^{3+}(SiP_2)_{dtet}{}^{2-}P_{plane}{}^{1-}$ as described for the $Pna2_1$ polymorph. However, if we assume the formation of P_2 dumbbells as predicted in calculations, we arrive at oxidation states of −2 for the P atoms in the pnictogen layer.

Summarizing the results of phonon calculations, optimized synthetic profiles, as well as *ex situ* and *in situ* annealings, the following thermal stability of the three polymorphs of $LaSiP_3$ can be deduced: $Pna2_1 \rightarrow P2_1/c \rightarrow Aea2$. It is peculiar that the low-temperature and high-temperature polymorphs in this sequence are closely related in structure, while the intermediate polymorph has a completely different arrangement of chemical bonds. While the intermediate polymorph can be bypassed in fast *in situ* experiments (going directly from $Pna2_1$ to $Aea2$), *ex situ* annealings performed for several days clearly show formation of the $P2_1/c$ polymorph at 900 °C. For $CeSiP_3$, the polymorphic relations are simplified by absence of the $P2_1/c$ polymorph: $Pna2_1 \rightarrow Aea2$.

^{31}P and ^{31}P{^{139}La} solid state NMR

Solid-state ^{31}P NMR spectroscopy was applied to distinguish the different phosphorus environments present in the different $LaSiP_3$ polymoprhs. Despite the use of fast-magic-angle-spinning (fast-MAS, ν_r = 36 kHz), sideband overlap was a challenge due to the wide spectral bandwidths and large chemical shift anisotropy found in these samples. As such, magic-angle-turning (MAT),[40,41] using the 5π sequence,[42] was applied to separate the anisotropic and isotropic components of the chemical shift tensors and obtain purely isotropic ^{31}P NMR spectra.

We first describe the results obtained for the $Pna2_1$ polymorph (structure with labeled P atoms is given in Fig. S9†). In the ^{31}P MAS spectrum of $LaSiP_3$ $Pna2_1$, there are a large number of resonances, in agreement with the six sites found in its crystal structure (Fig. 7a(i)). The spectrum is somewhat simplified with the use of MAT where we are able to further identify the six isotropic resonances (see Table S2†). To assign them, we performed gauge-including projector augmented-wave (GIPAW) density functional theory (DFT) calculations of the ^{31}P magnetic shielding tensors which were later converted to chemical shifts using the shielding calculated for GaP as a secondary reference (see ESI† for details). Notably, these calculations predicted that the P2 and P4 sites, which terminate the SiP_4 tetrahedral layers and are coordinated by La atoms, would have the greatest chemical shift anisotropy (Table S2†) which is in agreement with their assignment to the higher frequency resonances that have the most intense spinning sidebands.

The general placement of the resonances is only in moderate agreement with the experimental chemical shifts. There are three most likely causes for the disagreement: the relatively simple consideration of relativistic effects in our calculations, the known deficiency of PBE in describing empty La 4f orbitals,[43,44] and the sensitivity to slight changes in the energy levels of the conduction bands, which shares the same root cause as the band gap problem, *vide supra.*[45] The first two causes, in particular, are expected to significantly affect the calculated shieldings of phosphorus atoms surrounded by lanthanum. As such, we turned to the measurement of inter-

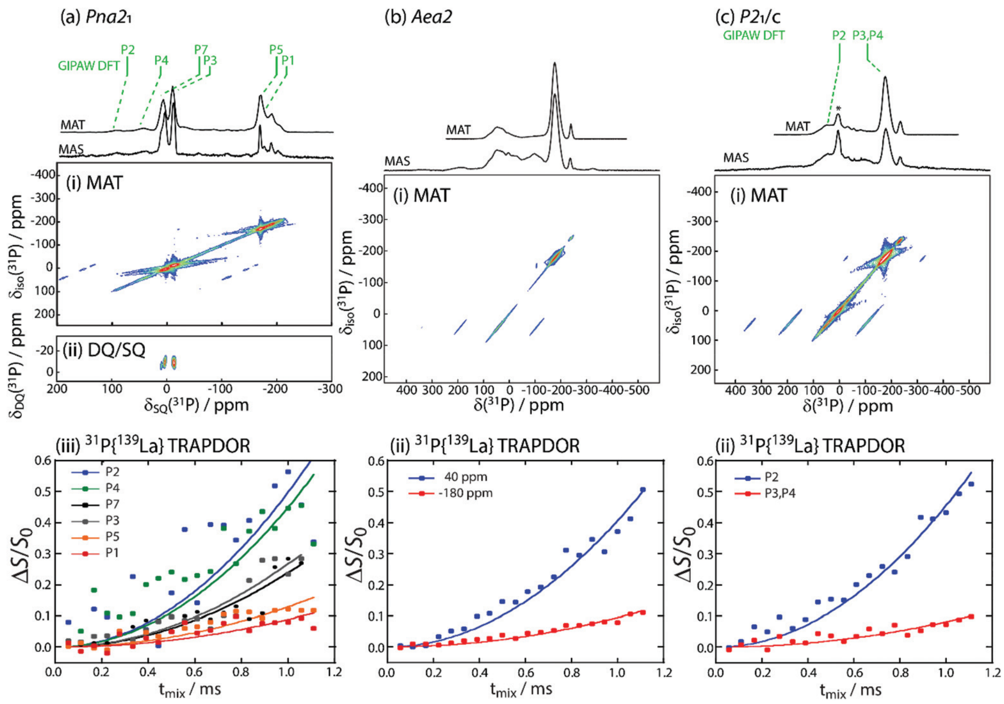

Fig. 7 Solid-state ^{31}P NMR data acquired for the (a) *Pna*2$_1$, (b) *Aea*2, (c) and *P*2$_1$/c polymorphs of LaSiP$_3$. The top traces show overlays of the ^{31}P MAS spectra, acquired with a rotor-synchronized echo experiment, and the projections of the isotropic dimensions of a 2D MAT experiment, also shown in (i). GIPAW-DFT-predicted ^{31}P chemical shifts are also marked in green above the spectra in (a) and (c). A DQ/SQ spectrum could be acquired for the *Pna*2$_1$ polymorph (ii) using the BaBa recoupling scheme. The bottom plots show the initial rise of ^{31}P{^{139}La} TRAPDOR experiments and their corresponding assignments to the different crystallographic crystal sites. * in (c)(i) denotes LaP impurity.

nuclear proximities to verify these assignments. Using the back-to-back (BaBa)[46] homonuclear double-quantum dipolar recoupling sequence, we were able to obtain a ^{31}P double-quantum-single-quantum (DQ/SQ) correlation spectrum, Fig. 7a(ii), which showed only a single correlation between the sites at −12 and 5 ppm. Based on the DFT results, these sites would correspond to the P3 and P7 sites, respectively, which are found in the phosphorus chains originating from Peierls distortion of the square P layer. As these sites form the only direct P–P bonds, the DQ/SQ spectrum confirms their assignments.

We then probed ^{31}P–^{139}La proximities using a transfer of population double-resonance (TRAPDOR)[47,48] experiment to differentiate the sites from the La-rich and Si-rich layers. This experiment requires the acquisition of echo datasets as a function of the echo delay both with and without the inclusion of ^{139}La irradiation. Irradiation at the ^{139}La Larmor frequency led to the recoupling of ^{31}P–^{139}La dipolar interactions and an attenuation of the echo signal. Data are commonly shown with the difference in intensity between these two experiments normalized to the regular echo intensity ($\Delta S/S_0$), Fig. 7a(iii). The initial dephasing is well described by a parabola, with the second-order rate constant being proportional to the sum-squared dipolar couplings ($\sum R_{\mathrm{DD}}^2$) between the two nuclides.[49–54] We observed that the higher frequency resonances dephased significantly faster (0.497 ms^{-2} and 0.449 ms^{-2}) than the lower frequency resonances (0.129 ms^{-2} and 0.089 ms^{-2}), with the P3 and P7 sites dephasing at intermediate rates of 0.239 ms^{-2} and 0.267 ms^{-2}. This is in good agreement with the $\sum R_{\mathrm{DD}}^2$ values for the three environments (250 973 s^{-2}, 56 950 s^{-2}, and 186 449 s^{-2}), confirming the GIPAW-DFT assignments of the phosphorus sites from the La-rich layer (P2 and P4) to the higher frequency resonances and those from the Si-rich layer (P5 and P1) to the lower frequency resonances.

The ^{31}P MAS and MAT spectra for the *Aea*2 polymorph (Fig. 7b) featured considerable overlap and far greater chemical shift anisotropy, in agreement with this polymorph's highly disordered structure (structure with labeled P atoms is given in Fig. S9†). Only two environments are resolved in the MAT projection, centered around −175 and 46 ppm. The peak at 46 ppm, however, does have an uneven lineshape suggesting the presence of multiple resonances. Unfortunately, the ^{31}P signals dephased too rapidly to enable acquisition of a ^{31}P DQ/SQ correlation spectrum, which would have confirmed the location of the terminal site in SiP$_4$ layer, P2. The ^{31}P{^{139}La} TRAPDOR experiment was nevertheless successful and showed the two resonances dephasing at rates of 0.405 ms^{-2} and 0.094 ms^{-2}, Fig. 7b(ii), thus identifying the resonance at the higher chemical shift to the La-rich layer, in agreement with that observed in the *Pna*2$_1$ polymorph. A closer inspection of the TRAPDOR spectra revealed that the higher frequency maximum, centered at 46 ppm, dephased significantly faster than the shoulder around −17 ppm (most clearly seen in the echo spectrum, Fig. 7b), suggesting that this shoulder belongs to the phosphorus layer sites, P2, in good agreement with their chemical shift in the *Pna*2_1 polymorph. Note that the similarity of the ^{31}P chemical shifts from the phosphorus layers in both the *Pna*2_1 and *Aea2* polymorphs strongly suggests that the *Aea2* polymorph also features infinite P fragments as opposed to the isolated P_2 dumbbells resulting from the DFT optimizations.

We lastly studied the monoclinic polymorph that crystalizes in the *P*2_1/c space group (structure with labeled P atoms is given in Fig. S10†). This polymorph featured two main resonances, namely a sharp resonance at −172 ppm and a broader one at 42 ppm (Fig. 7c). Additional resonances correspond to impurities present in the sample. GIPAW DFT calculations predicted that the P2 site from the La-rich layer would again resonate at the higher chemical shift while the P3 and P4 sites would have nearly identical lower frequency chemical shifts. These assignments were confirmed by the ^{31}P{^{139}La} TRAPDOR measurement which showed the fastest dephasing for the 42 ppm resonance (Fig. 7c(iii)). The room-temperature spin–lattice-T_1 relaxation times for the three polymorphs were of 2.2 s for all sites in *Aea*2, 4.1 and 3.4 s for high and low frequency signals in *P*2_1/*c*; and 26.5, 11.1 and 39.2 s for the three regions from high to low frequency in *Pna*2_1 (Table S2 and Fig. S9, 10†). The magnitude of T_1 relaxation times suggest all three polymorphs are semiconductors.

Transport properties

Measurements of the resistivities and thermal conductivities of the *Ln*SiP$_3$ (*Ln* = La and Ce) phases were performed on highly compacted polycrystalline sintered samples (Fig. 8). All four phases exhibit a semiconducting behavior with resistivity increasing with decreasing temperature. This agrees with T_1 relaxation times from solid-state NMR studies of LaSiP$_3$ polymorphs (Table S2†), thus disproving the computational prediction of metallic behavior in *Aea*2. Diffuse reflectance measurements further support the semiconducting nature of the LaSiP$_3$ polymorphs with both non-centrosymmetric polymorphs having similar direct bandgaps of 0.97(1) eV (*Pna*2_1) and 0.96(1) eV (*Aea*2), while the significantly different crystal structure of the monoclinic polymorph (*P*2_1/*c*) results in larger bandgap of 1.23(1) eV (Fig. 8). Below 150 K for LaSiP$_3$ (*Aea*2) and both CeSiP$_3$ samples, and below 325 K for LaSiP$_3$ (*Pna*2_1) sample, resistivity measurements become unreliable (cross-section and cooling/heating rate dependent) and such data are not shown. Based on computations and the smaller NMR relaxation times for the LaSiP$_3$ *Aea*2 polymorph as compared to *Pna*2_1 polymorph, one can expect that the *Aea*2 phases have higher carrier concentrations. Indeed, for both rare-earth metals studied, either La or Ce, the resistivity of the completely ordered *Pna*2_1 polymorph is higher than that for the disordered *Aea*2 forms (Fig. 8).

For the thermal conductivities, we expect the disordered nature of P layers coupled with additional minor disorder in the Si–P layer to reduce the thermal conductivity for *Aea*2 polymorphs. This was indeed observed with both *Pna*2_1 polymorphs having higher thermal conductivities than the *Aea*2 polymorphs (Fig. 8). Moreover, the disorder present in the P layers in *Aea*2 polymorphs resulted in glass-like behavior of the thermal conductivity with gradual increase of the thermal con-

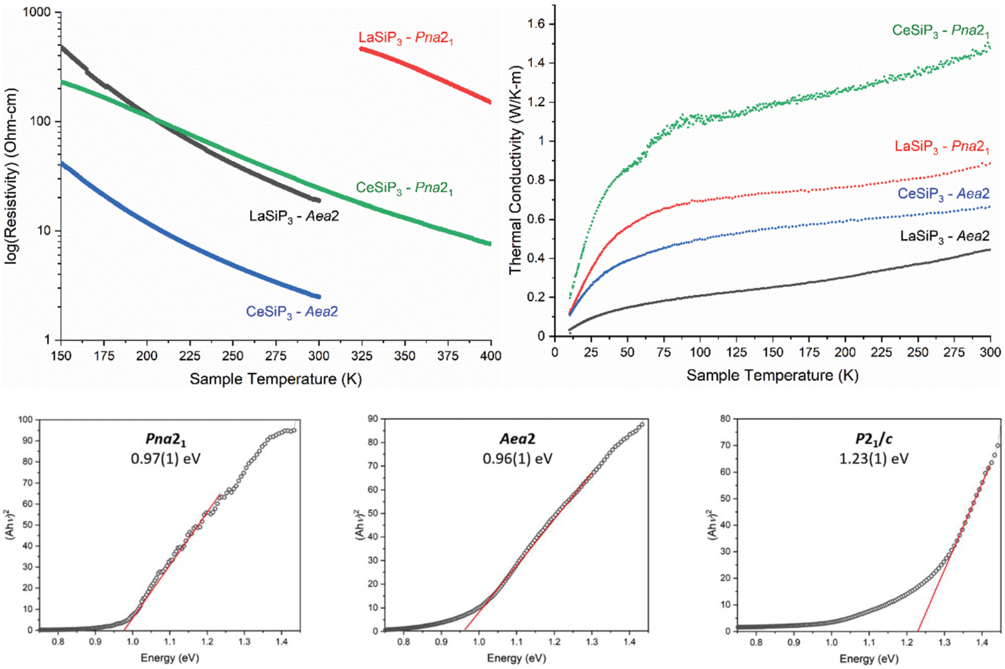

Fig. 8 (Top) Transport properties of *Ln*SiP$_3$ (*Ln* = La and Ce) for *Pna*2_1 and *Aea*2 polymorphs: (left) electrical resistivity (right) and thermal conductivity. (Bottom) Tauc plots for the direct transitions for all three LaSiP$_3$ polymorphs.

ductivity over a wide temperature range. Overall, the studied phases exhibit quite low thermal conductivity for the crystalline samples in the range of 0.4–1.6 W m^{-1} K^{-1} at room temperature. Complex non-centrosymmetric semiconductors with high thermal stability and low thermal conductivity might be a useful platform for the development of thermoelectric materials assuming the carrier concentration is tunable. Studies of various aliovalent substitutions to modify the carrier concentrations of these phases are currently underway.

Conclusions

The synthesis and characterization of five *Ln*SiP$_3$ compounds (*Ln* = La and Ce) are presented: *Pna*2$_1$, *Aea*2, and *P*2$_1$/*c* polymorphs for LaSiP$_3$; and *Pna*2$_1$ and *Aea*2 polymorphs for CeSiP$_3$. The synthesis of these phases involved a novel method of atomically mixing the refractory components (*Ln* + Si) *via* arc-melting and then reacting the precursor with elemental P. *In situ* studies reveal that the main advantage of this method is direct conversion of *Ln*Si to ternary *Ln*SiP$_3$ phase, bypassing the formation of SiP – a common by-product of the reaction from the elements. This study emphasizes the value of the proposed synthetic method as it allows to overcome solid–solid diffusion and reactivity limitations. The developed synthetic method is widely applicable for systems with conflicting reactivities of the components.

The structures of the *Pna*2$_1$ and *Aea*2 polymorphs are similar with alternating layers of lanthanide, [SiP$_2$] double tetrahedral, and phosphorus layers (2D distorted square nets of P for *Aea*2 and 1D *cis–trans* chains of P for *Pna*2$_1$). The P local environments were confirmed using Raman spectroscopy and advanced solid-state NMR methods, including the measurement of ^{31}P–^{31}P and ^{31}P–^{139}La proximities. Electronic DOS calculations predicted semiconducting behavior for the *P*2$_1$/*c* and *Pna*2$_1$ polymorphs, and phonon DOS calculations supported that these two polymorphs are dynamically stable with a predicted and experimentally-verified phase transformation from the *Pna*2$_1$ to the *P*2$_1$/*c* polymorph. Several computational models were constructed to study the disordered *Aea*2 polymorph but did not accurately depict the semiconducting behavior observed from properties. Transport properties measurements and diffuse reflectance spectroscopy showed the *Pna*2$_1$ and *Aea*2 polymorphs for both La and Ce are semiconductors with bandgaps of less than 1 eV. Ultra-low thermal conductivities at room temperature were observed for the *Aea*2 polymorphs which feature highly disordered P layers. Studies of the tunability of non-centrosymmetric P layers for further studies of the topological and electronic properties of these complex materials is currently underway.

Author contributions

The manuscript was written through contributions of all authors.

Funding sources

G. A. is grateful to the Ames Laboratory Spedding Postdoctoral Fellowship for financial support. B. C. M. is thankful to the Jonathan and Susan Rich Undergraduate Research Scholarship and ISU LAS Dean's High Impact Undergraduate Research Award for financial support. This work was supported by the Ames Laboratory's Laboratory Directed Research and Development (LDRD) program (G. A., J. M., G. V, J. W., S. J. L., K. K.). F. Z., C.-Z. W., and K.-M. H. were supported by the U.S. Department of Energy (DOE), Office of Science, Basic Energy Sciences, Division of Materials Science and Engineering, including computer time support on National Energy Research Scientific Computing Center (NERSC) in Berkeley, CA. Solid-state NMR work (F. A. P. and A. P.) was supported by the U.S. Department of Energy (DOE), Office of Science, Basic Energy Sciences, Materials Science and Engineering Division. The Ames Laboratory is operated for the U.S. DOE by Iowa State University under contract #DE-AC02-07CH11358. Use of the Advanced Photon Source at Argonne National Laboratory was supported by the U. S. Department of Energy, Office of Science, Office of Basic Energy Sciences, under Contract No. DE-AC02-06CH11357.

Conflicts of interest

Authors declare no conflict of interests.

Acknowledgements

We thank Prof. J. V. Zaikina (ISU) for access to the SPS and UV/Vis/NIR spectrophotometer, and Prof. V. Pecharsky (ISU and Ames Laboratory) for access to the arc-melting setup. We thank the beamline scientists Dr S. Lapidus, Dr A. Yakovenko, and Dr W. Xu for the help in data collection at the 11-BM and 17-BM beamlines at the Advanced Photon Source at Argonne National Laboratory.

References

1 K. Watanabe, T. Taniguchi and H. Kanda, Direct-Bandgap Properties and Evidence for Ultraviolet Lasing of Hexagonal Boron Nitride Single Crystal, *Nat. Mater.*, 2004, **3**(6), 404–409, DOI: 10.1038/nmat1134.

2 Y. Tian, B. Xu, D. Yu, Y. Ma, Y. Wang, Y. Jiang, W. Hu, C. Tang, Y. Gao, K. Luo, Z. Zhao, L.-M. Wang, B. Wen, J. He and Z. Liu, Ultrahard Nanotwinned Cubic Boron Nitride, *Nature*, 2013, **493**(7432), 385–388, DOI: 10.1038/nature11728.

3 R. T. Paine and C. K. Narula, Synthetic Routes to Boron Nitride, *Chem. Rev.*, 1990, **90**(1), 73–91, DOI: 10.1021/cr00099a004.

4 Y. Kubota, K. Watanabe, O. Tsuda and T. Taniguchi, Deep Ultraviolet Light-Emitting Hexagonal Boron Nitride

Synthesized at Atmospheric Pressure, *Science*, 2007, **317**(5840), 932–934, DOI: 10.1126/science.1144216.

5 V. L. Solozhenko, O. O. Kurakevych and Y. Le Godec, Creation, of Nanostuctures by Extreme Conditions: High-Pressure Synthesis of Ultrahard Nanocrystalline Cubic Boron Nitride, *Adv. Mater.*, 2012, **24**(12), 1540–1544, DOI: 10.1002/adma.201104361.

6 N. Dubrovinskaia, V. L. Solozhenko, N. Miyajima, V. Dmitriev, O. O. Kurakevych and L. Dubrovinsky, Superhard Nanocomposite of Dense Polymorphs of Boron Nitride: Noncarbon Material Has Reached Diamond Hardness, *Appl. Phys. Lett.*, 2007, **90**(10), 101912, DOI: 10.1063/1.2711277.

7 B. Owens-Baird, J. Xu, D. Y. Petrovykh, O. Bondarchuk, Y. Ziouani, N. González-Ballesteros, P. Yox, F. M. Sapountzi, H. Niemantsverdriet, Y. V. Kolen'ko and K. Kovnir, NiP_2: A Story of Two Divergent Polymorphic Multifunctional Materials, *Chem. Mater.*, 2019, **31**(9), 3407–3418, DOI: 10.1021/acs.chemmater.9b00565.

8 A. Haffner and D. Johrendt, Synthesis, Crystal Structure, and, Chemical Bonding of Ba_2SiP_4: Synthesis, Crystal Structure, and Chemical Bonding of Ba_2SiP_4, *Z. Anorg. Allg. Chem.*, 2017, **643**(21), 1717–1720, DOI: 10.1002/zaac.201700320.

9 A. Haffner, V. Weippert and D. Johrendt, Polymorphism of Ba $_2$ SiP $_4$: Polymorphism of Ba $_2$ SiP $_4$, *Z. Anorg. Allg. Chem.*, 2020, **646**(3), 120–124, DOI: 10.1002/zaac.201900188.

10 V. Sousa, B. F. Gonçalves, M. Franco, Y. Ziouani, N. González-Ballesteros, M. Fátima Cerqueira, V. Yannello, K. Kovnir, O. I. Lebedev and Y. V. Kolen'ko, Superstructural Ordering in Hexagonal CuInSe $_2$ Nanoparticles, *Chem. Mater.*, 2019, **31**(1), 260–267, DOI: 10.1021/acs.chemmater.8b04368.

11 A. F. Moodie and H. J. Whitfield, Determination of the Structure of Cu $_2$ ZnGeS $_4$ Polymorphs by Lattice Imaging and Convergent-Beam Electron Diffraction, *Acta Crystallogr., Sect. B: Struct. Sci.*, 1986, **42**(3), 236–247, DOI: 10.1107/S0108768186098282.

12 A. S. R. Chesman, J. van Embden, E. Della Gaspera, N. W. Duffy, N. A. S. Webster and J. J. Jasieniak, Cu $_2$ ZnGeS $_4$ Nanocrystals from Air-Stable Precursors for Sintered Thin Film Alloys, *Chem. Mater.*, 2014, **26**(19), 5482–5491, DOI: 10.1021/cm501393h.

13 S. Ono, H. Hayakawa and K. Nomura, Synthesis of Ln-Si-P (Ln=La, Ce, Pr) Ternary Compounds, *J. Chem. Soc. Jpn.*, 1976, **11**, 1700–1709.

14 H. Hayakawa, T. Sekine and S. Ono, Chemical Transport Reactions of Some Rare Earth Phosphides: Syntheses of New Rare Earth-Silicon-Phosphorus Ternary Compounds, *J. Less-Common Met.*, 1975, **41**(2), 197–210, DOI: 10.1016/0022-5088(75)90028-4.

15 H. Hayakawa, S. Ono and A. Kobayashi, The Crystal Structure of Cerium Silicon Triphosphide (CeSiP3), *J. Chem. Soc. Jpn.*, 1978, **9**, 1214–1220.

16 S. Klemenz, S. Lei and L. M. Schoop, Topological Semimetals in Square-Net Materials, *Annu. Rev. Mater. Res.*, 2019, **49**(1), 185–206, DOI: 10.1146/annurev-matsci-070218-010114.

17 S. Klemenz, A. K. Hay, S. M. L. Teicher, A. Topp, J. Cano and L. M. Schoop, The Role of Delocalized Chemical Bonding in Square-Net-Based Topological Semimetals, *J. Am. Chem. Soc.*, 2020, **142**(13), 6350–6359, DOI: 10.1021/jacs.0c01227.

18 P. Kaiser and W. Jeitschko, The Rare Earth Silicon Phosphides LnSi2P6(Ln = La, Ce, Pr, and Nd), *J. Solid State Chem.*, 1996, **124**(2), 346–352, DOI: 10.1006/jssc.1996.0248.

19 J. Mark, J. Wang, K. Wu, J. G. Lo, S. Lee and K. Kovnir, $Ba_2Si_3P_6$: 1D Nonlinear Optical Material with Thermal Barrier Chains, *J. Am. Chem. Soc.*, 2019, **141**(30), 11976–11983, DOI: 10.1021/jacs.9b04653.

20 J. Mark, J.-A. Dolyniuk, N. Tran and K. Kovnir, Crystal and Electronic Structure and Optical Properties of AE_2 SiP $_4$ (*AE* = Sr, Eu, Ba) and $Ba_4Si_3P_8$: Crystal and Electronic Structure and Optical Properties of AE_2 SiP_4 (*AE* = Sr, Eu, Ba) and $Ba_4Si_3P_8$, *Z. Anorg. Allg. Chem.*, 2019, **645**(3), 242–247, DOI: 10.1002/zaac.201800430.

21 J.-A. Dolyniuk, D. C. Kaseman, S. Sen, J. Zhao, F. E. Osterloh and K. Kovnir, *MP*-BaP_3: A New Phase from an Old Binary System, *Chem. – Eur. J.*, 2014, **20**(34), 10829–10837, DOI: 10.1002/chem.201305078.

22 K. E. Woo, J. Wang, K. Wu, K. Lee, J.-A. Dolyniuk, S. Pan and K. Kovnir, Mg-Si-As: An Unexplored System with Promising Nonlinear Optical Properties, *Adv. Funct. Mater.*, 2018, **28**(30), 1801589, DOI: 10.1002/adfm.201801589.

23 D. Rutzinger, C. Bartsch, M. Doerr, H. Rosner, V. Neu, T. Doert and M. Ruck, Lattice Distortions in Layered Type Arsenides LnTAs2 (Ln=La–Nd, Sm, Gd, Tb; T=Ag, Au): Crystal Structures, Electronic and Magnetic Properties, *J. Solid State Chem.*, 2010, **183**(3), 510–520, DOI: 10.1016/j.jssc.2009.12.021.

24 X. Lin, S. S. Stoyko and A. Mar, Ternary Rare-Earth Zinc Arsenides REZn2As3 (RE=La–Pr) Containing Defect Fluorite-Type Slabs, *J. Solid State Chem.*, 2013, **199**, 189–195, DOI: 10.1016/j.jssc.2012.12.026.

25 A. Mills, Chains, Planes, and Antimonides, *Coord. Chem. Rev.*, 2002, **233–234**, 207–222, DOI: 10.1016/S0010-8545(02)00097-8.

26 G. A. Papoian and R. Hoffmann, Hypervalent Bonding in One, Two, and Three Dimensions: Extending the Zintl-Klemm Concept to Nonclassical Electron-Rich Networks, *Angew. Chem., Int. Ed.*, 2000, **39**, 2408–2448, DOI: 10.1002/1521-3773(20000717)39:14<2408::aid-anie2408>3.0.co;2-u.

27 R. Troc, J. Leciejewicz and R. Ciezewski, Antiferromagnetic Structure of Uranium Diphosphide, *Phys. Status Solidi*, 1966, **15**, 515–519.

28 S. I. Chihrii, Synthesis and Crystal Structure of SmCuP2 Compound, *Zh. Neorg. Khim.*, 1990, **35**, 1656–1658.

29 G. Akopov, G. Viswanathan and K. Kovnir, Synthesis, Crystal and Electronic Structure of La2SiP4, *Z. Anorg. Allg. Chem.*, 2020, **647**, 91, DOI: 10.1002/zaac.202000378.

30 J. Wang, J. Mark, K. E. Woo, J. Voyles and K. Kovnir, Chemical Flexibility of Mg in Pnictide Materials: Structure

and Properties Diversity, *Chem. Mater.*, 2019, **31**(20), 8286–8300, DOI: 10.1021/acs.chemmater.9b03740.

31 B. Eisenmann, H. Jordan and H. Schäfer, Ba3Si4P6, Eine Neue Zintlphase Mit Vernetzten Si4P5-Käfigen/On Ba3Si4P6, a New Zintl Phase with Connected Si4P5 Cages, *Z. Naturforsch., B: Anorg. Chem., Org. Chem.*, 1984, **39**(7), 864–867, DOI: 10.1515/znb-1984-0705.

32 B. Eisenmann, H. Jordan and H. Schäfer, Zintl-phasen mit komplexen anionen: Darstellung und struktur der o-phosphosilikate und -germanate EII4EIVP4 (MIT EII = Ca, Sr, Ba und EIV = Si, Ge), *Mater. Res. Bull.*, 1982, **17**(1), 95–99, DOI: 10.1016/0025-5408(82)90188-X.

33 J. Wang, Y. He, N. E. Mordvinova, O. I. Lebedev and K. Kovnir, The Smaller the Better: Hosting Trivalent Rare-Earth Guests in Cu–P Clathrate Cages, *Chem*, 2018, **4**(6), 1465–1475, DOI: 10.1016/j.chempr.2018.04.001.

34 W. Tremel and R. Hoffmann, Square Nets of Main-Group Elements in Solid-State Materials, *J. Am. Chem. Soc.*, 1987, **109**(1), 124–140, DOI: 10.1021/ja00235a021.

35 X. Zhang, J. Li, B. Foran, S. Lee, H.-Y. Guo, T. Hogan, C. R. Kannewurf and M. G. Kanatzidis, Distorted Square Nets of Tellurium in the Novel Quaternary Polytelluride K0.33Ba0.67AgTe2, *J. Am. Chem. Soc.*, 1995, **117**(42), 10513–10520, DOI: 10.1021/ja00147a012.

36 R. Patschke, J. Heising, J. Schindler, C. R. Kannewurf and M. Kanatzidis, Site Occupancy Wave and Unprecedented Infinite Zigzag (Te2–2)NChains in the Flat Te Nets of the New Ternary Rare Earth Telluride FamilyALn3Te8, *J. Solid State Chem.*, 1998, **135**(1), 111–115, DOI: 10.1006/jssc.1997.7606.

37 C. D. Malliakas and M. G. Kanatzidis, Charge Density Waves in the Square Nets of Tellurium of *AMRE* Te$_4$ (*A* = K, Na; *M* = Cu, Ag; *RE* = La, Ce), *J. Am. Chem. Soc.*, 2007, **129**(35), 10675–10677, DOI: 10.1021/ja073986m.

38 C. Malliakas, S. J. L. Billinge, H. J. Kim and M. G. Kanatzidis, Square Nets of Tellurium: Rare-Earth Dependent Variation in the Charge-Density Wave of RETe$_3$ (RE = Rare-Earth Element), *J. Am. Chem. Soc.*, 2005, **127**(18), 6510–6511, DOI: 10.1021/ja0505292.

39 R. Patschke and M. G. Kanatzidis, Polytelluride Compounds Containing Distorted Nets of Tellurium, *Phys. Chem. Chem. Phys.*, 2002, **4**(14), 3266–3281, DOI: 10.1039/b201162j.

40 N. M. Szeverenyi, A. Bax and G. E. Maciel, Magic-Angle Hopping as an Alternative to Magic-Angle Spinning for Solid State NMR, *J. Magn. Reson. (1969)*, 1985, **61**(3), 440–447, DOI: 10.1016/0022-2364(85)90184-2.

41 Z. Gan, High-Resolution Chemical Shift and Chemical Shift Anisotropy Correlation in Solids Using Slow Magic Angle Spinning, *J. Am. Chem. Soc.*, 1992, **114**(21), 8307–8309, DOI: 10.1021/ja00047a062.

42 J. Z. Hu, D. W. Alderman, C. Ye, R. J. Pugmire and D. M. Grant, An Isotropic Chemical Shift-Chemical Shift Anisotropy Magic-Angle Slow-Spinning 2D NMR Experiment, *J. Magn. Reson.*, 1993, **105**, 82–87.

43 M. Profeta, M. Benoit, F. Mauri and C. J. Pickard, First-Principles Calculation of the ^{17}O NMR Parameters in Ca Oxide and Ca Aluminosilicates: The Partially Covalent Nature of the Ca–O Bond, a Challenge for Density Functional Theory, *J. Am. Chem. Soc.*, 2004, **126**(39), 12628–12635, DOI: 10.1021/ja0490830.

44 A. Sadoc, M. Body, C. Legein, M. Biswal, F. Fayon, X. Rocquefelte and F. Boucher, NMR Parameters in Alkali, Alkaline Earth and Rare Earth Fluorides from First Principle Calculations, *Phys. Chem. Chem. Phys.*, 2011, **13**(41), 18539, DOI: 10.1039/c1cp21253b.

45 R. Laskowski, P. Blaha and F. Tran, Assessment of DFT Functionals with NMR Chemical Shifts, *Phys. Rev. B: Condens. Matter Mater. Phys.*, 2013, **87**(19), 195130, DOI: 10.1103/PhysRevB.87.195130.

46 M. Feike, D. E. Demco, R. Graf, J. Gottwald, S. Hafner and H. W. Spiess, Broadband Multiple-Quantum NMR Spectroscopy, *J. Magn. Reson., Ser. A*, 1996, **122**(2), 214–221, DOI: 10.1006/jmra.1996.0197.

47 C. P. Grey and W. S. Veeman, The Detection of Weak Heteronuclear Coupling between Spin 1 and Spin l/2 Nuclei in MAS NMR; 14N/' 3C/'H Triple Resonance Experiments, *Chem. Phys. Lett.*, 1992, **192**(4), 7.

48 C. P. Grey and J. Vega, Determination of the Quadrupole Coupling Constant of the Invisible Aluminum Spins in Zeolite HY with 1H/27Al TRAPDOR NMR, *J. Am. Chem. Soc.*, 1995, **117**, 8232–8242.

49 J. C. C. Chan and H. Eckert, Dipolar Coupling Information in Multispin Systems: Application of a Compensated REDOR NMR Approach to Inorganic Phosphates, *J. Magn. Reson.*, 2000, **147**(2), 170–178, DOI: 10.1006/jmre.2000.2191.

50 M. Bertmer and H. Eckert, Dephasing of Spin Echoes by Multiple Heteronuclear Dipolar Interactions in Rotational Echo Double Resonance NMR Experiments, *Solid State Nucl. Magn. Reson.*, 1999, **15**(3), 139–152, DOI: 10.1016/S0926-2040(99)00050-8.

51 M. Bertmer, L. Züchner, J. C. C. Chan and H. Eckert, Short and Medium Range Order in Sodium Aluminoborate Glasses. 2. Site Connectivities and Cation Distributions Studied by Rotational Echo Double Resonance NMR Spectroscopy, *J. Phys. Chem. B*, 2000, **104**(28), 6541–6553, DOI: 10.1021/jp9941918.

52 W. Strojek, M. Kalwei and H. Eckert, Dipolar NMR Strategies for Multispin Systems Involving Quadrupolar Nuclei: 31P{ ^{23} Na} Rotational Echo Double Resonance (REDOR) of Crystalline Sodium Phosphates and Phosphate Glasses, *J. Phys. Chem. B*, 2004, **108**(22), 7061–7073, DOI: 10.1021/jp037041c.

53 W. Strojek and H. Eckert, Medium-Range Order in Sodium Phosphate Glasses: A Quantitative Rotational Echo Double Resonance Solid State NMR Study, *Phys. Chem. Chem. Phys.*, 2006, **8**(19), 2276, DOI: 10.1039/b518080e.

54 S.-J. Huang, S.-B. Liu and J. C. C. Chan, Heteronuclear Dipolar Recoupling of Half-Integer Quadrupole Nuclei under Fast Magic Angle Spinning, *Solid State Nucl. Magn. Reson.*, 2009, **36**(2), 110–117, DOI: 10.1016/j.ssnmr.2009.07.002.